Formation of OH(v=0,1) by the Reaction of Fast H with O_3

James A. Dodd,* Ronald B. Lockwood, Eunsook S. Hwang,† Steven M. Miller, and Steven J. Lipson

Air Force Research Laboratory, Space Vehicles Directorate, Hanscom Air Force Base, Massachusetts 01731-3010, and Stewart Radiance Laboratory, Bedford, Massachusetts

Received: June 21, 1999; In Final Form: August 2, 1999

A two-laser, pump−probe experiment has been used to determine the rotational level population distribution of OH(v=0,1) resulting from the reaction of fast (2.3 eV) hydrogen atoms with ozone. A trace amount of H_2S in slowly flowing O_3 was photolyzed at 193 nm, and the resultant OH was detected using laser-induced fluorescence (LIF). The pump−probe delay time was adjusted in order to verify negligible relaxation of the nascent OH product. Initially, side reactions such as $O(^1D) + H_2S \rightarrow OH + HS$ were found to contribute to the OH signals; they were subsequently eliminated by adjusting the reactant concentrations and flow velocity. The resultant OH LIF spectra were corrected for several factors using either known or measured experimental quantities, including OH(A) collisional quenching, baseline drift, and partial saturation of the OH(A−X) absorption lines. Near-gas kinetic rate constants for OH(A,v'=0,$N' \leq 25$) collisional quenching by O_3 were derived. The corrected spectra were fit using a nonlinear least-squares routine to infer individual N-level populations for OH(v=0,1). The spin−orbit (F_1 and F_2) and λ-doublet ($\Pi(A')$ and $\Pi(A'')$) populations were inferred in a separate least-squares fit by comparing the intensities of different OH(A−X) rotational branches. The OH v=1:v=0 population ratio is equal to 0.37 ± 0.04. For both v levels the rotational level populations increase gradually with N, with the population in $N = 20$ about 5 times that in $N = 1$. The F_1:F_2 and $\Pi(A')$:$\Pi(A'')$ population ratios are equal to 1.03 ± 0.28 and 1.34 ± 0.20, respectively.

Introduction

The influences of the reaction

$$H + O_3 \rightarrow OH(v \leq 9) + O_2 + 3.35\ \text{eV} \qquad (1)$$

in the mesopause region of 85−90 km are manifold. Reaction 1 gives rise to the well-known OH Meinel airglow bands extending from the visible into the infrared. These bands result from vibration−rotation emission in the fundamental and strong overtone bands of the OH product. The Meinel bands have been observed using a large number of instruments and techniques from both ground- and space-based sensors. Recent examples of the latter include the WINDII imaging interferometer experiment aboard the UARS satellite,[1] the CIRRIS 1A infrared emission experiment on the space shuttle,[2] and the UVISI stellar-occultation[3] and SPIRIT III high-resolution interferometer[4] experiments, both aboard the MSX satellite.

A significant development in recent years has been the observation and characterization of highly excited OH (v=0−3) rotational populations in the mesopause region. In the CIRRIS 1A experiment OH populations in levels up to $N = 33$, with rotational energies ≤2.3 eV, were inferred from pure rotation emissions in the 10−25 μm region.[2] Those observations have since been corroborated by similar measurements from the SPIRIT III interferometer.[4] Very recently, excited OH rotational populations in $v = 4$−10 have been inferred from ground-based Keck telescope data.[5] It is not known whether the high-N populations are formed directly through reaction 1, or through a secondary energy transfer process, such as resonant vibration-to-rotation transfer from nascently formed high-v levels.[2] The question of the origin of the low v level populations is important in terms of the dynamic nature of reaction 1.

The nascent OH vibrational distribution has been measured by a number of workers.[6−9] All of these studies made use of OH Meinel emission for detection and are in general agreement that the nascent vibrational populations are highly inverted, peaking at $v = 9$, which is the highest level allowed from the available reaction energy of 27 000 cm^{-1}. The reported measurements extend down to various v levels, the lowest being $v = 3$ in the infrared chemiluminescence experiment of Charters et al.[9] However, none of these studies reports any yield information for OH(v=0−2), and the most recent experimental study of Klenerman and Smith[6] probed only $v \geq 6$. Thus, in spite of the importance of the $H + O_3$ reaction in the mesopause region, the lowest v levels of the nascent OH product have received almost no attention in the measurements described in the literature.

In our initial study of reaction 1, we report the vibration−rotation population distribution in OH(v=0,1) from the reaction of translationally excited ("fast") H atoms with ozone. The experiment was carried out in a room-temperature, gas-phase mixture of H_2S and O_3. Laser photolysis was used to stimulate the following reaction sequence:

$$H_2S + h\nu(193\ \text{nm}) \rightarrow H^* + HS \qquad (2)$$

$$H^* + O_3 \rightarrow OH + O_2 \qquad (3)$$

The photolysis (2) is an efficient source of H atoms owing to the large H_2S absorption cross section and near-unit dissociation quantum yield at 193 nm. The nascently produced hydrogen atoms, denoted H*, are highly translationally excited, with an

† Stewart Radiance Laboratory.

10.1021/jp992051s CCC: $18.00
Published on Web 09/11/1999

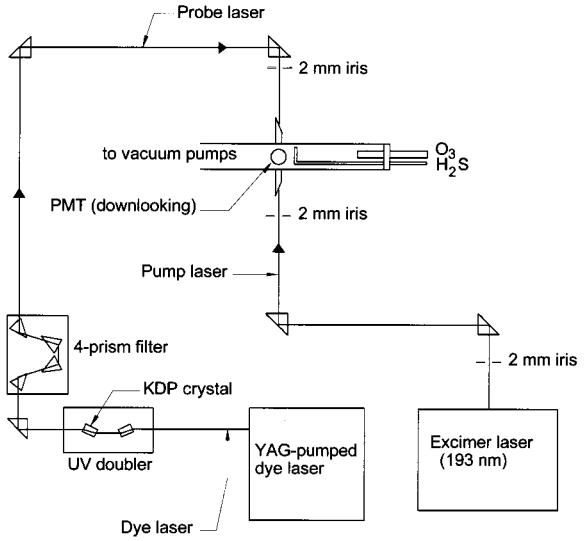

Figure 1. A schematic of the experimental apparatus used in the laser photolysis−laser probe experiment for generating and detecting OH-(v=0,1) from H* + O_3 → OH + O_2.

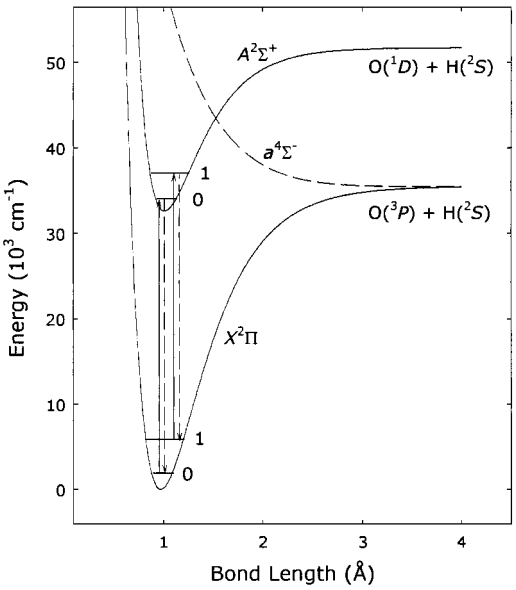

Figure 2. OH(A $^2\Sigma^-$−X $^2\Pi$) laser-induced fluorescence detection scheme. The A−X (0−0) and (1−1) bands shown are excited by the probe laser, then resonantly detected in the 308−320 nm region. The OH(a $^4\Sigma^-$) state is largely responsible for the OH(A $^2\Sigma^-$) state predissociation, which affects levels above approximately $N = 26$ in $v' = 0$ and $N = 16$ in $v' = 1$.

average kinetic energy of 2.3 eV.[10,11] Our study provides new information concerning the OH low-v product channels of reaction 3, both for the rotational level distribution and also for the distribution among the four possible λ-doublet states. The measured product distributions should also serve as a useful benchmark to help validate and improve the H−O_3 potential energy surfaces used in trajectory studies.[12,13]

Experimental Section

Apparatus. An outline of the experimental apparatus is shown in Figure 1. The flow tube assembly consists of a 21 cm long, 4.5 cm internal diameter glass tube, coated on its internal surface with halocarbon wax to reduce the decomposition of the ozone. Clamped to the downstream end of the flow tube is the reaction cell, composed of an aluminum cube bored through to give the same 4.5 cm internal diameter, and black-anodized on its internal surfaces. The cell was specially machined in order to closely maintain the circular cross section of the flow tube and minimize turbulence effects. A shelf was machined into the cell body to allow a 2.54 cm diameter, *f*/1 lens to be positioned 2.5 cm above the laser interaction region. This lens greatly improves the species detection limits. Fused-silica windows of 3.8 cm diameter are mounted on the upper and lower cell faces. Two 21 cm long black-anodized aluminum sidearm assemblies are attached for passage of the laser light. Each sidearm contains six or seven blackened (Ebonol-coated) brass light baffles, with the laser entrance and exit windows mounted at Brewster's angle in order to minimize window scatter from the horizontally polarized probe laser beam. The gases were pumped by a Leybold-Heraeus Ruvac WS1000 Roots blower, backed by Heraeus-Engelhard DK 180 roughing pump, with the line constricted to achieve the desired pumping speed. The reaction cell pressure was monitored using a 10 Torr full-range MKS Baratron capacitance manometer.

Ozone was produced by flowing oxygen through a commercial ozonator, and stored on about 650 g of 3−8 mesh silica gel in a glass trap cooled to −75 °C. After ozonating for several hours, the trap was pumped on to remove the bulk of the residual O_2; it was pumped on again just prior to data-taking. During the experiment the O_3 was allowed to flow into the flow cell under its own backing pressure, about 10 Torr. The O_3 was passed through a Teflon valve to meter the flow rate, then through about two meters of $^1/_4''$ o.d. Teflon tubing into the reaction flow tube. The O_3 density in the foreline was continually monitored via the absorption of 292.5/296.7 nm Hg lamp emission with a monochromator−phototube arrangement, and the Teflon valve was occasionally adjusted to maintain the desired concentration. The O_3 flow was estimated to be 22 standard cm^3 min^{-1} based on an Ar flow producing an equivalent pressure rise. The ozone was found to be 95 ± 5% pure at the cell by comparing the Baratron readings with 253.7 nm Hg-lamp absorption measurements, indicating minimal decomposition in the glass and Teflon foreline. Neat hydrogen sulfide (Matheson, 99.5%) was introduced through a loop injector 1 cm upstream of the laser interaction region at a flow rate of 0.5 standard cm^3 min^{-1}, giving rise to a 2% mixture of H_2S in O_3. The total pressure of 280 mTorr corresponded to a linear flow velocity of 55 cm s^{-1}.

Photolysis pulses were generated by a Lambda-Physik Lextra 200 excimer laser, operating at 193 nm and a 10 Hz repetition rate. A pair of irises (see Figure 1) removed the off-axis light and simplified the optical alignment. Fluences of about 100 μJ were used, corresponding to photon flux densities of 3×10^{15} cm^{-2}. Probe pulses were generated using a Spectra-Physics PDL-2 dye laser loaded with DCM dye, pumped in the longitudinal mode by a 10 Hz Spectra-Physics DCR-2A Nd:YAG laser. The dye laser output pulses were frequency doubled using an Inrad Autotracker II equipped with a compensated KDP crystal. The counterpropagating probe beam was overlapped with the photolysis beam using the series of irises. The resultant OH(v=0,1) rotational populations were monitored by scanning the A−X (0−0) and (1−1) bands in the 308−330 nm region, and detecting the resonant emission using a 1P21 photomultiplier tube fitted with an 11 nm fwhm, 307 nm center wavelength band-pass filter. Figure 2 shows the probe scheme utilizing the OH(A−X) transitions. Relatively high probe fluences of about 60 μJ were used for adequate sensitivity for detecting the small resultant signals, with the signals corrected for partial saturation (see below). The probe laser bandwidth was about 0.7 cm^{-1}, substantially larger than the absorption Doppler width of about

TABLE 1: Absorption Cross Sections for O_3 and H_2S at Several Laser Wavelengths (in 10^{-19} cm^2)

wavelength (nm)	$\sigma(O_3)^a$	$\sigma(H_2S)^b$
193	4.28	69
248	108.0	0.40
266	96.5	0.0067

[a] Reference 27. [b] Reference 40.

0.1 cm^{-1}. The laser wavelength step increment was 0.0029 nm in the visible, corresponding to 0.001 45 nm, or approximately 0.15 cm^{-1}, in the ultraviolet. A relative spectral calibration of the 1P21 phototube−band-pass filter combination was performed using a factory-calibrated Optronics M-626 tungsten lamp in conjunction with a scanning 3 nm fwhm monochromator and a 100 Hz chopper.

The observed OH signals were prompt, appearing within about 20 ns after the photolysis pulse. The signals used to derive the OH populations were typically detected at about 100 ns delay time, in order to minimize residual signal from the 193 nm photolysis pulse. About 0.1 gas-kinetic collisions have occurred between the parent molecules in the time between H* creation and OH detection. The H atoms are produced from H_2S photolysis with about 2.3 eV of translational energy, corresponding to a velocity of 2.1×10^6 cm s^{-1}. The H−O_3 gas-kinetic collision time at this velocity is a few tens of nanoseconds, suggesting that there could be a contribution to the OH signals from partially thermalized H atoms. However, time-delay scans of several representative transitions showed that the corresponding OH populations did not increase significantly between 30 and 150 ns, suggesting that they are largely the product of a single collision between nascent H* and O_3. The observation is also consistent with negligible OH collisional relaxation.

The raw PMT output signals were passed to an EG&G Ortec 535 fast current amplifier, and then to an SRS SR250 gated integrator, with time gates ranging between 10 and 100 ns. The signals were digitized using an SRS SR245 12-bit analog-to-digital converter and the data transferred over an IEEE-488 interface to a PC. LabVIEW 4.0, running on the PC, was used to control the wavelength scan and to store the digitized data stream. The subsequent numerical analysis was carried out on a Digital Equipment Corporation AlphaStation 250.

Elimination of Side Processes. At the 193 nm photolysis wavelength, the photolytic cross section for H-atom production from H_2S is 16 times larger that for O(^{1}D) production from O_3 (see Table 1). However, the small amount of O(^{1}D) which is generated through O_3 photolysis at 193 nm will react efficiently with H_2S *via*

$$O(^1D) + H_2S \rightarrow OH(v \leq 6) + HS + 2.44\ eV \qquad (4)$$

The OH(v) nascent distribution arising from reaction 4 has a broad maximum in the $v = 1-4$ region.[14] The extent to which reaction 4 contributed to the signal was probed in two ways. First, the O_3-H_2S mixture was photolyzed at 266 nm, at a high enough fluence to produce several times the predicted O(^{1}D) number density arising from 193 nm photolysis. The H_2S photolytic cross section at 266 nm is far lower than that of O_3 (Table 1), and reaction 3 can be neglected. Second, the photolysis laser was blocked, and the probe laser was tuned to the $R_1(5)$ transition of the A−X 0−0 band at 306.7 nm, closer to the O_3 Hartley band. This method purposely photolyzed some of the O_3 to produce O(^{1}D), with the OH product from reaction 4 detected in the same pulse. No OH signal could be detected using either method when flowing a trace amount of H_2S in excess O_3, indicating that reaction 4 was essentially eliminated.

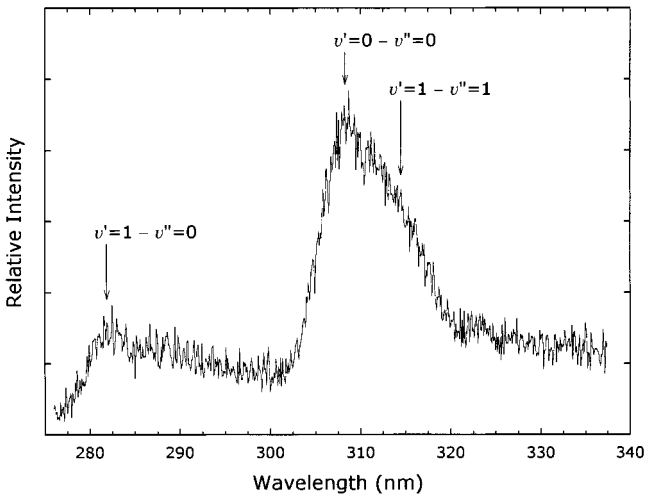

Figure 3. Chemiluminescence from the OH(A) excited state, which is stimulated under certain pressure and flow conditions in H_2S-O_3 mixtures by either 193, 248, or 266 nm excitation. Emission from $v' = 0,1$ is clearly visible in the spectrum. This signal was largely eliminated under the experimental conditions used to obtain the OH-(X,v=0,1) laser-induced fluorescence data.

At slow flow velocities, i.e. 3.7 cm s^{-1}, some OH(v=0,1) signal remains when either of the O_3 or H_2S flows is interrupted. When H_2S is absent, the signal probably arises from the small amount of O(^{1}D) generated through 193 nm photolysis reacting with trace hydrocarbon impurities present in the flow tube. At faster flow speeds (55 cm s^{-1}), however, these signals were completely absent within the limits of the signal-to-noise ratio (S/N). The faster flow used a copious amount of O_3; thus the storage column was fully loaded and maintained at a higher temperature, about −65 °C, in order to achieve an adequate backing pressure.

It is also conceivable that the observed OH signals resulted from the reaction of H with a trace amount of O_2 present in the O_3 flow, *viz.*

$$H^* + O_2 + 0.72\ eV \rightarrow OH + O \qquad (5)$$

Although reaction 5 is endothermic, it can be driven by the 2.3 eV translational energy of the nascent H atom arising from H_2S photolysis.[15] To check for the presence of reaction 5, variable amounts of O_2 were added to the O_3 flow, with no change in the signal intensity. No signal was observed with only H_2S and O_2 present.

Finally, under certain conditions of the gas partial pressures, firing only the 193 nm excimer laser was found to stimulate fluorescence in the 307 nm region. This fluorescence could be mitigated by either increasing or decreasing the H_2S mole fraction. The fluorescence was present using either the O_3-H_2S mixture or an O_3-H_2 mixture, and using 193, 248, or 266 nm excitation. It was not observed using 355 nm excitation, suggesting a key role for O(^{1}D) in initiating the reaction sequence giving rise to the fluorescence. Studies utilizing a low-resolution monochromator to disperse the fluorescence showed that it was consistent with the formation of OH(A,$v' \leq 1$), with emission being observed at 282 nm and at 308 nm (see Figure 3). Another group has evidence that the OH(A) is formed from energy-pooling reactions of vibrationally excited OH(X).[16] Since the OH(A) chemiluminescence grows in and decays on a time scale of about 10 μs, it was discriminated against by probing at delay times closely following the photolysis pulse (i.e., 100 ns).

TABLE 2: Experimental Conditions Used To Reduce or Eliminate Spurious Sources of OH(v=0,1)

spurious signal	possible source	remedy
OH(v=0,1) LIF signal with 248 nm or 266 nm excitation	$O(^1D) + H_2S \rightarrow OH + HS$	used a trace amount of H_2S in excess O_3
OH(v=0,1) LIF signal with only H_2S or O_3 present	$O(^1D) + RH \rightarrow OH + R$[a]	increased flow velocity from 3.7 to 55 cm s^{-1}
OH(A) chemiluminescence signal with 193, 248, or 266 nm excitation	OH(X,v) energy pooling	used a trace amount of H_2S in excess O_3; detected OH prior to chemiluminescence signal

[a] RH represents a trace hydrocarbon impurity.

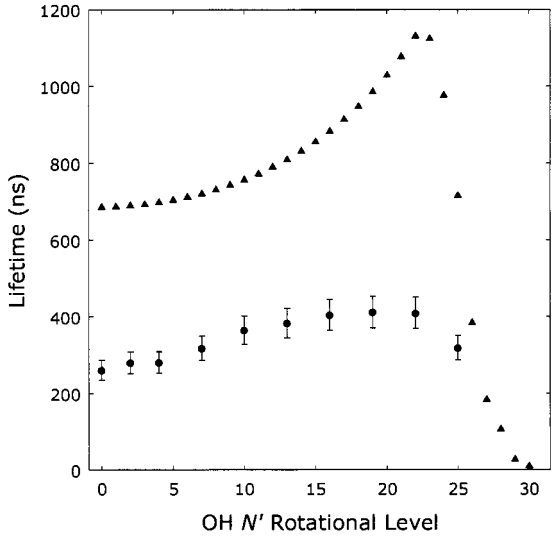

Figure 4. OH(A $^2\Sigma^-$, v=0) lifetimes as a function of the rotational level N'. The circles are the measurements for 280 mTorr of O_3 containing a trace of H_2S, while the triangles are the collision-free lifetimes from Luque and Crosley.[17]

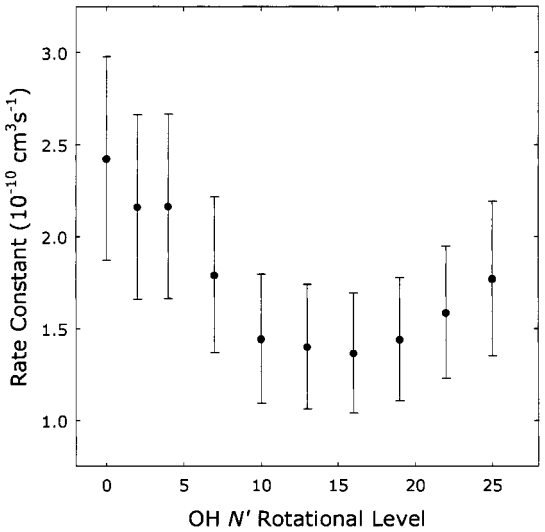

Figure 5. Rate constants for the collisional quenching of OH(A $^2\Sigma^-$, v=0) by O_3, derived from measurements including those shown in Figure 4. The error bars are the statistical 2σ values.

The small H_2S partial pressure served to largely eliminate the OH(A) chemiluminescence signal.

A description of the various spurious signals, their possible origin, and the experimental conditions ultimately used to reduce or eliminate them is presented in Table 2.

Collisional Quenching of OH(A). At the 280 mTorr cell pressure, the OH(A) lifetimes were found to be significantly shorter than the literature radiative lifetimes. Due to the strong influence of collisional quenching in determining the OH(A) radiative quantum yields and thus the derived OH(X) populations, the OH(A,v=0,1;N) lifetimes were measured for several O_3 pressures. Small probe fluences were used to mitigate the effects of window scatter. A LeCroy 9310AM 400-MHz, 100 MS s^{-1} digital oscilloscope monitored the time during which the fluorescence amplitude decayed from 80% to 20% of its maximum, avoiding both the short-lived laser scatter and any nonexponential long-time behavior. The lifetimes was negligibly broadened by the stated 1P21 phototube and Ortec 535 preamplifier instrumental rise times of 2.2 ns and <3 ns, respectively. Figure 4 shows that the measured lifetimes for $v' = 0$ are significantly smaller than the literature collision-free lifetimes.[17] Aside from the high-N, predissociated levels, the disappearance rates for the F_1 and F_2 spin-rotational manifolds and for $v' = 0$ and $v' = 1$ were found to be identical within the experimental error. For $v' = 1$, this suggests that electronic quenching dominates over vibrational relaxation. The quenching is governed by collisions with O_3, as indicated by the fact that the lifetimes were found to be approximately inversely proportional to the O_3 density. The derived O_3 quenching rate constants as a function of N' are shown in Figure 5. To our knowledge, they represent the first rate constant measurements for OH(A) electronic quenching by O_3.

Boxcar Gate Width Effects. Owing to the collision-shortened lifetimes, the dependence of the derived populations on the boxcar gate width was also investigated. The derived populations were found to continuously evolve on lowering the gate widths from 100 ns down to 30 ns. The populations did not vary provided the gate width was maintained below about 30 ns, notwithstanding the poor S/N in the 10 and 20 ns data. In fact, for small gate widths the derived populations are relatively insensitive to the O_3-induced collisional quenching, as shown in the following. For a given OH(v',N') fluorescing upper state population, the corresponding OH(v'',N'') lower state population is proportional to

$$\Phi C_{\text{gate}} = \left(\frac{\tau_{\text{coll}}}{\tau_{\text{rad}}}\right)\left(1 - \exp\left(\frac{-\tau_{\text{gate}}}{\tau_{\text{coll}}}\right)\right) \approx \left(\frac{\tau_{\text{coll}}}{\tau_{\text{rad}}}\right)\left(\frac{\tau_{\text{gate}}}{\tau_{\text{coll}}}\right) = \frac{\tau_{\text{gate}}}{\tau_{\text{rad}}} \quad (6)$$

In eq 6, Φ is the fluorescence quantum yield, C_{gate} is a correction factor which accounts for the finite gate width, τ_{coll} is the collision-limited lifetime, τ_{rad} is the radiative lifetime, and τ_{gate} is the instrumental gate width. If $\tau_{\text{gate}}/\tau_{\text{coll}}$ is small, the exponential can be approximated using the first term in the Taylor expansion as shown in eq 6. The collisional lifetime τ_{coll} drops out in this approximation, and the quantum yield-gate width correction is determined solely through the instrument setting and literature radiative lifetimes. A similar equation holds for the highest N' values, in which the A state becomes partially predissociated.

At the 280 mTorr total pressure, hard-sphere collisions occur about every microsecond, while OH(A) rotational state-changing collisions may occur more often, owing to long-range attractive forces. As mentioned above, there is no evidence that the derived populations are altered by lowering the gate width below 30 ns, implying that the initial laser-excited OH(v',N') populations are not significantly redistributed during the detection period. Thus, the detection sensitivity for a given rotational transition was taken to be proportional to the product of the Einstein A coefficient and the relative spectral response at the appropriate

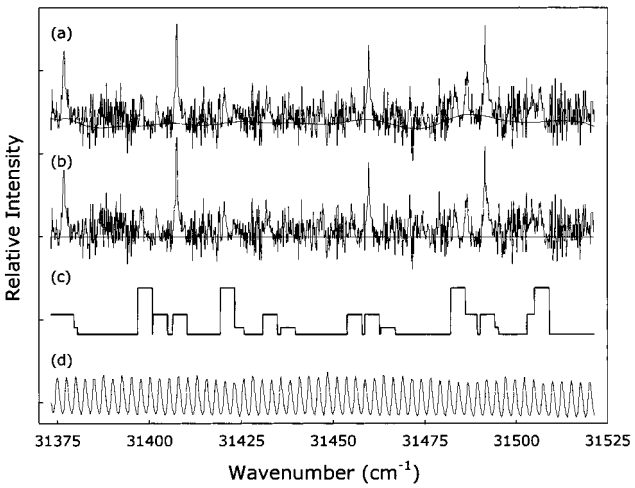

Figure 6. (a) OH($A\ ^2\Sigma^- - X\ ^2\Pi$) laser-induced fluorescence spectrum, together with the baseline obtained using the robust estimate technique. (b) The spectrum obtained after baseline subtraction. (c) Number of laser shots used to obtain each data point, ranging from 8 to 64 in powers of 2. The scanning program performs more averaging in the vicinity of an OH LIF transition. The baseline estimation and least-squares fitting routines weight the data points according to the square root of the number of laser shots. (d) The etalon trace used to linearize the wavenumber values. The typical best-fit value of the free spectral range of the etalon equals 1.27 cm^{-1} at the visible dye laser wavelength near 635 nm.

wavelength, summed over the downward transitions from a given initially excited OH(v',N') level. This includes the six fully allowed P_1, P_2, Q_1, Q_2, R_1, and R_2 branches, as well as the six satellite branches which have significant intensity for low-N values.

Data Acquisition and Reduction

Acquisition. Individual scans were obtained consisting of 1000 data points, spanning about 150 cm^{-1}. At the beginning of each scan, a Burleigh WA5500 pulsed wavemeter was used to determine the dye laser wavenumber value for later use in the least-squares fit. After a scan was obtained, the two lasers and the detection apparatus were checked and adjusted if necessary, and another scan initiated without changing the position of the probe laser wavelength. Thus, over several hours of data-taking a series of scans was obtained that could be concatenated into a single, global OH A−X (0−0) and (1−1) spectrum. All of the observed lines were identified as OH(A−X) transitions. Much of the time spent scanning is consumed by the "dead space" between the OH lines, especially in the P-branch regions. In order to minimize the necessary data acquisition time, the laser was scanned slowly in the vicinity of an OH line, with up to 64-shot averaging, and quickly when not near an OH line. The current wavenumber value was estimated by the LabVIEW data-taking program using the initial wavenumber value and the approximate step size. The level of averaging for a sample scan is shown in Figure 6. Although the spectrum in Figure 6 appears to be noisy, the OH lines were actually obtained with far better S/N than is apparent from the scan.

Wavenumber Linearization. In the initial spectral fits, the wavenumber positions of the data and model OH lines could not be made to coincide by adjusting the offset or the scaling of the model spectrum wavenumber values. The problem arises from the PDL-2 dye laser: we found that the wavelength could not be reliably predicted from the grating step number owing to nonlinearities in the drive mechanism. To address this issue, a small portion of the visible dye laser beam was directed through an external etalon and onto a Si photodiode. With the laser scanning, this provided laser fringes at a spacing corresponding to approximately 1.27 cm^{-1} in the visible. The fringe signal is shown at the bottom of Figure 6. This data channel was stored on the PC along with the other channels and used to linearize the spectrum as described in the following.

The fringe signal was first smoothed using the Savitsky−Golay algorithm, with a 25-point smoothing window and a fourth-order polynomial fitting function.[19] The first derivative output was used to eliminate the signal dc offset. Zero crossings were then located by fitting the three points nearest each zero crossing to a linear function. Finally, the OH LIF data points were assigned channel numbers corresponding to the zero crossings, with points occurring between zero crossings linearly interpolated and assigned fractional fringe numbers.[20] Spectral fits to scans linearized in this manner gave rise to residuals that completely lacked the derivative character observed in the nonlinearized scans, indicating that the data and model line positions were well aligned.

Baseline Correction. A complication arose from the baseline in the LIF spectra, which was observed to vary over a time scale of minutes. The baseline drift did not seem to correlate with any experimental observables, e.g. the photolysis or probe laser fluences, or the O_3 concentration. However, the drift, if uncorrected, would adversely affect the accuracy of the derived OH populations. Thus, it was necessary to develop an estimate of the baseline for subtraction from the data. This was performed using a robust fitting technique similar to that described by Jacobson.[21] In robust estimation a merit function is chosen that is insensitive to outlier points, in contrast to the standard least-squares fitting methods, which strongly weight the outliers. Spectra were fit to a polynomial using the following merit function:

$$\sum_i z_i^k (1 - e^{-z_i^2/2}) \tag{7}$$

where

$$z_i = \frac{y_i - f_i}{\sigma_i} \tag{8}$$

In eq 8, y_i and f_i are the data and model values for point i, respectively, and σ_i is an estimate of the uncertainty. The uncertainties σ_i were taken to be proportional to the inverse of the square root of the number of laser shots, with the overall scaling estimated from the rms scatter in the intensities not in the vicinity of an OH transition.

The data were first fit to eq 7 with $k = 2$, giving a merit function which closely resembles χ^2, the standard least-squares fitting function. The fit was then iterated by decreasing k in steps of 0.2, which "anneals" the function over to one more typical of robust estimation. Each fit was applied to a subset of 150 contiguous data points within each 1000-point scan, with the second half of each subset overlapped with the first half of the next. The subsets cut off near the end points of the 1000-point scan were extended by reflecting the values about a y-axis placed at the appropriate endpoint. The overlapping estimates were then coadded using a triangular weighting function, with unit weight in the center of each 150-point subset and zero weight at the outer points. Figure 6 shows the baseline thus determined for a small portion of the data, along with the corrected data obtained by subtracting the baseline. The baseline estimation method will be detailed in a forthcoming publication.[22]

Modeling Partially Saturated LIF Spectra. Increasing the probe laser fluence to 60 μJ was found to greatly improve the S/N, with the obvious advantage of allowing much more precise derived OH populations. However, this fluence level has the disadvantage of partially saturating the fully allowed OH(A−X) absorption lines, requiring a more complex interpretation of the observed signals. In order to estimate the extent of saturation, trial spectra were obtained using only the probe laser, together with a cw microwave discharge source of OH(v=0). Hydrogen atoms were formed from a dilute mixture of H_2 in Ar passed through a 30 W microwave discharge, and a trace amount of NO_2 was injected downstream to foster the reaction

$$H + NO_2 \rightarrow OH + NO \tag{9}$$

OH(A−X) 0−0 LIF spectra were obtained by scanning near 310 nm, and collecting all of the fluorescence in the 0−0 emission band using a coarse monochromator in conjunction with a phototube. A 60 μJ spectrum was obtained to replicate the data-taking conditions and a 3 μJ spectrum to provide a benchmark, unsaturated case. The 60 μJ data were found to be power-broadened by a few percent relative to the 3 μJ data. Between the two spectra the observed peak intensity ratios varied by a maximum of about 50%. At 3 μJ, the observed spectra could be quantitatively modeled by assuming an unsaturated spectrum and a 295 K distribution of OH(v=0) rotational level populations.

To interpret the 60 μJ data, a simple saturation model was developed, with the only adjustable parameter corresponding to the effective laser pumping rate. The LIF signal is proportional to the upper state population, here denoted as N_f, present at the termination of the probe laser pulse. Under low fluence conditions, N_f is in turn proportional to the lower state population N_i. During the laser pulse, the rate of change of the populations N_f and N_i is given by[23]

$$\frac{dN_f}{dt} = \rho B_{abs} N_i - \left(\rho B_{emi} + \frac{1}{\tau_{rad}} + k_{coll}[M]\right) N_f \tag{10}$$

$$\frac{dN_i}{dt} = -\rho B_{abs} N_i + (\rho B_{emi} + A_{fi}) N_f \tag{11}$$

where ρ is the radiant energy density, B_{abs} and B_{emi} are the Einstein absorption and stimulated emission coefficients, respectively, τ_{rad} is the upper state radiative lifetime, $k_{coll}[M]$ is the collisional quenching rate resulting from a rate constant k_{coll} and a gas density [M], and A_{fi} is the Einstein coefficient connecting the upper and lower levels. In a cw system, it is straightforward to assume steady-state conditions for the upper and lower state populations, set eq 10 equal to zero, and solve for N_f as a function of the saturation parameter S

$$S = \frac{\rho B_{abs}}{\frac{1}{\tau_{rad}} + k_{coll}[M]} \tag{12}$$

However, in the case of a pulsed laser the system does not generally reach equilibrium, even at fast excitation rates; i.e., the populations are continuing to evolve even as the probe laser shuts off. The steady-state assumption is obviously incorrect in this case.

In order to estimate the population N_f following the laser pulse, eqs 10 and 11 were numerically integrated in time steps of 100 ps over the 10 ns laser pulse duration. Most of the parameters in eqs 10 and 11 are well-known, including the Einstein A and B coefficients and the radiative lifetimes. The collisional quenching rates were found to be small and were neglected. The radiant energy density ρ was then adjusted in the integration of eqs 10 and 11 until the model spectrum bore a close resemblance to the data. The method was checked by comparing the unsaturated 3 μJ data to the model obtained using small values of ρ; an excellent match was obtained. For the 60 μJ data, the best-fit value of ρ corresponds to pumping rates near 10^7 s^{-1} for the strongest lines, consistent with the estimated average probe flux density of 10^{23} cm^{-2} s^{-1} and the maximum absorption cross sections of 10^{-16} cm^2. This analysis enabled the model spectrum to correctly reproduce the intensity ratio of lines with absorption coefficients differing by up to a factor of 10.

Obviously, this method is only approximate, since it ignores factors such as the spatial and temporal variation of the laser beam intensity. In our experiment, however, the spatial dependence of the laser intensity is expected to be minimal, since the probe beam is passed through an iris that selects the centermost portion of the beam. The effective value of ρ is necessarily time-averaged over the laser pulse duration, as the temporal dependence of the laser intensity would be difficult to model with any precision. Nevertheless, we consider this treatment to be significantly more accurate than a model which assumes either an unsaturated spectrum or one that is totally saturated. The best-fit value of ρ from the 60 μJ trial data was used together with eqs 10 and 11 to generate effective OH(A−X) absorption coefficients for interpreting $H^* + O_3$ spectra.

Doppler-Broadening of OH Line Widths. In the spectral data the low-N transitions were noticeably broadened, by about 0.5 cm^{-1}, relative to the high-N transitions. As mentioned above, the power broadening at 60 μJ is minimal, and the dye laser does not have a significant bandwidth variation over the wavelength region scanned. All of the peaks exhibited a Gaussian line shape. The observation is consistent with increased Doppler broadening in the low-N levels, which nominally have a greater percentage of the reaction energy available for translation. The population of $N = 25$, for instance, requires about 1.5 eV of rotational energy that would otherwise be available to feed into the relative velocity of the $OH + O_2$ products. The broadening was modeled as a function of N, with the translational energy available to the OH E_{avail} taken to be

$$E_{avail} = E_{rxn} - E_v - E_N \tag{13}$$

In eq 13, E_{rxn} is the energy released from the reaction, and E_v and E_N are vibrational and rotational energy, respectively. The quantity E_{rxn} was taken to be the sum of the reaction exothermicity (3.3 eV) and the energy of the fast H atom (2.3 eV). The resultant Doppler broadening was calculated from E_{avail} assuming that the nascent OH product molecule has no preferred direction of travel relative to the probe laser beam. The model reproduced the observed broadening to within the S/N of the data, which is typically small for the high-N levels. While the broadening is quite apparent, the data do not have sufficient S/N to further quantify the effect, such as in fitting for E_{rxn} in an attempt to characterize the amount of energy channeled into the O_2 internal degrees of freedom. The OH(v,N) populations were derived taking into account the N-dependent line-shape variation.

Least-Squares Spectral Fitting. Nonlinear least-squares fits were performed to determine OH(v=0,1) populations from the OH(A−X) LIF spectra. OH(A−X) spectral basis functions were generated using OH(X) and OH(A) term values taken from Melen et al.[24] and Coxon,[25] respectively. The calculated

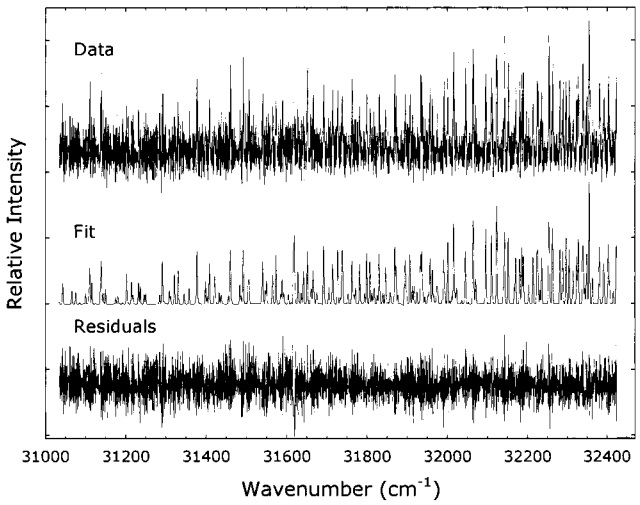

Figure 7. Baseline-corrected OH(A $^2\Sigma^-$−X $^2\Pi$) laser-induced fluorescence data, obtained on one of the days of scanning, together with the model spectrum from the nonlinear least-squares fit and the corresponding residuals. Note that a minimum of averaging is performed between OH transitions, resulting in data which appear to be noisy, while not affecting the precision of the best-fit parameters.

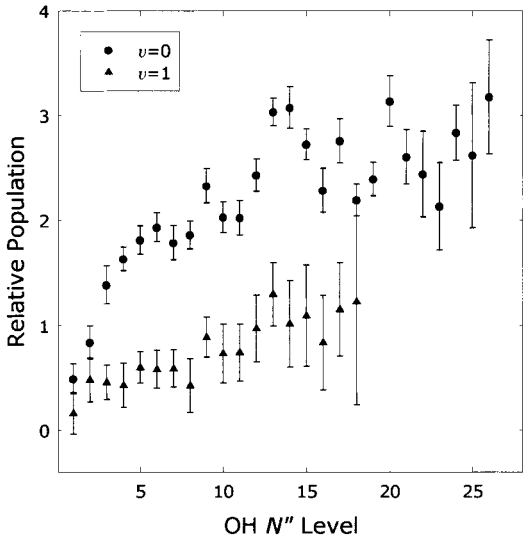

Figure 8. OH(X $^2\Pi$) *N*-level nascent populations from the reaction of fast H* with O_3, derived from nonlinear least-squares spectral fits to data like those shown in Figure 7. The populations are seen to increase with *N*. The v=1:v=0 ratio for the *N* levels detected in this study is equal to 0.37 ± 0.04. The error bars are the statistical 2σ values.

frequencies were found to agree with those of Luque and Crosley[17] to better than 0.01 cm^{-1}, and well within the bandwidth of the probe laser. The line intensities were calculated using literature absorption coefficients,[17,18] modified by the partial saturation model described above. The lines were then convolved with a Gaussian line-shape function. Details such as the OH(A) *N*-dependent collision-limited lifetimes, the duration of the boxcar gate, and the relative spectral response function of the detection system were included in the model as described above. The spectra were fit using the Levenberg−Marquardt nonlinear least-squares method.[19] The fit was repeated with many different starting conditions in order to test for the presence of secondary minima on the χ^2 surface. No other minimum was found, adding confidence to the validity of our result.

In the course of the analysis, several 1000-point scans were fit simultaneously to a set of global parameters, comprising of the OH(v=0,1;*N*) relative populations, the Gaussian full width at half-maximum Δ, and the etalon spacing γ, and to a set of local parameters which accommodated the wavelength offset of each individual scan. In the fitting process, best-fit frequency positions were obtained by making first guesses for the initial wavenumber value and the fringe spacing, and then allowing the two parameters to vary in the fit. The fits typically succeeded provided the first guesses were within a few percent of the best-fit values. Figure 7 shows a typical data spectrum which has been corrected for baseline drift and nonlinearities in the wavelength as described above, along with the best-fit model spectrum and the residuals. As mentioned above, the scanning routine performs a great deal of averaging in the vicinity of an OH line, with less averaging between the lines, resulting in more efficient data-taking at the expense of a somewhat "noisier" looking spectrum.

Two different fits were performed to each set of data. In the first fit, it was assumed that for each *N* value the four λ-doublet populations are equal in population, and thus a single population was used for each *N* value. In the second fit, the populations in the four different λ-doublet states were fit individually. The λ-doublets are formed from the four possible combinations of the F_1 and F_2 spin−orbit levels and the Π(A′) and Π(A″) λ-doublet levels. The four populations are quite easily resolved, since the OH(A−X) selection rules dictate that each of the 12 bands probes only one of the four populations. For instance, the Π_1(A′) population is probed by the P_1 and R_1 branches, while the Π_1(A″) population is probed by the Q_1 branch. For the lowest *N* values, where the coupling between the orbital, electron spin, and rotational degrees of freedom is accurately described by Hund's case (a), the Π(A′) and Π(A″) states are not eigenstates of the OH Hamiltonian, but can be formally associated with the e and f eigenstates. As *N* increases, the angular momentum coupling changes over to Hund's case (b), which becomes an accurate description for $N > A/B = 7.7$, where *A* is the spin−orbit splitting and *B* is the rotational constant. In Hund's case (b), the λ-doublets are OH eigenstates, and they have a clear physical interpretation: in the Π(A′) state the orbital containing the unpaired O-atom electron is in the plane of rotation, while in the Π(A″) state the orbital is perpendicular to the plane of rotation.[26] Because the λ-doublets are a signature of the relative orientation of the electronic and mechanical degrees of freedom in the nascently produced molecule, they have been used to interpret the formation mechanism for the molecules in which they occur, most notably OH and NO.[2]

Results and Discussion

The OH(v=0,1) populations resulting from the fit assuming equal λ-doublet populations are shown in Figure 8. For both v levels, the rotational level populations increase gradually with *N*. The v=1:v=0 population ratio is equal to 0.37 ± 0.04, a value obtained by averaging over the rotational level populations that are determined for both v levels, roughly $N \leq 18$. For the second fit, in which the λ-doublet populations were allowed to vary independently, the χ^2 value was found to decrease about 10%, indicating a marginally better result. In this fit, since each population is being determined using only a subset of the rotational branches, the statistical uncertainties in the populations are larger than those shown in Figure 8, and too large to extract any meaningful results for $v = 1$. For $v = 0$, the overall F_1:F_2 and Π(A′):Π(A″) population ratios were determined by calculating the ratio for each *N* value, then averaging over all *N*, weighting each individual ratio inversely by its variance.

TABLE 3: Comparison of Measured OH(v=0,1;N,Ω,λ) Nascent Population Distribution from H* + O_3 → OH + O_2 and Related Reactions (Uncertainties Listed for the Present Work Are 2σ)

reaction	v=1:v=0	rotational distribution (v=0)	F_1:F_2	Π(A′):Π(A″)	reference
H* + O_3 → OH + O_2	0.37 ± 0.04	inverted[a]	1.03 ± 0.28	1.34 ± 0.20	present study
H* + O_2 → OH + O	0.47 ± 0.15	inverted[b]	1 ± 0.2	5.9 ± 1.0[c]	*d*
O(^{1}D) + H_2S → OH + HS	0.17 ± 0.03	2300 ± 100 K	1 ± 0.2	1 ± 0.2	*e*

[a] The population in $N = 20$ is about 5 times that in $N = 1$. [b] The population in $N = 20$ is about 20 times that in $N = 1$. [c] Increases with N, the ratio approaching 5.9 for the highest N levels probed (about $N = 25$). [d] Reference 15. [e] Reference 41.

Calculated in this manner, the average spin−orbit population ratio F_1:F_2 was found to equal 1.03 ± 0.28, indicating that the two populations are produced in equal yields. On the other hand, the λ-doublet population ratio Π(A′):Π(A″) was determined over the range $N = 7-27$ to equal 1.34 ± 0.20, indicating a significantly higher yield of the Π(A′) component.

Little information has been obtained regarding the λ-doublet distribution from the laboratory studies of the H + O_3 reaction, which have concentrated on the vibrational distribution.[6−9] This is probably at least partly due to the difficulty with which the λ-doublets are resolved while observing the OH Meinel band emission, which all of the experiments used to detect the OH. In the seminal Charters et al.[9] study, however, the authors determined a propensity for population of the F_1 spin−orbit state of up to a factor of 2 or more, for $N \leq 10$ of $v = 7-9$. No information has been obtained for the Π(A′):Π(A″) population ratio from the laboratory experiments. In the CIRRIS 1A space-shuttle observations of OH(v=0−3) pure rotation spectra, for $N = 13-33$, the F_1:F_2 and Π(A′):Π(A″) population ratios were determined as 1.0 ± 0.15 and 1.8 ± 0.3, respectively. However, it is unclear whether the low-v OH observed in the CIRRIS 1A experiment arises from reaction 1, or from a secondary process involving quenching of nascently formed OH(v=6−9).[2] It is also unclear whether the fast H atoms inherent in this study can serve as a suitable proxy for the thermalized H atoms present in the mesopause region near the 85 km altitude where the OH Meinel nightglow emission occurs.

Table 3 summarizes the results for the present study, and compares the results to the corresponding values for reactions 4 and 5. In general, the product OH(v,N,Ω,λ) populations determined in the three experimental studies differ. In the Kleinermanns et al.[15] study of the H* + O_2 reaction, the authors photolyzed HBr to form fast H atoms with 2.6 eV average translational energy, slightly higher than the 2.3 eV H-atom energy in the present experiment. Interestingly, all three studies observed equal amounts of the F_1 and F_2 spin−orbit populations. In other respects, the present results are more similar to the results for the H* + O_2 study than to those for O(^{1}D) + H_2S, with the notable exception of the λ-doublet distribution. In their study of H* + O_2, Kleinermanns et al.[15] observed for rotational levels approaching $N = 25$ that the Π(A′) λ-doublet is preferred by a factor of 6 over the Π(A″) λ-doublet, a much larger ratio than the average value of 1.3 obtained herein. The present data do not indicate any increase of the Π(A′):Π(A″) ratio with increasing N, to within the error bars in the individual population ratios.

The H + O_3 reaction is 27 000 cm^{-1} exothermic, with a measured activation barrier of only 330 ± 140 cm^{-1},[27] far less than the H-atom translational energy of 18 500 cm^{-1} in the present experiment. While the yield of OH in higher v levels relative to $v = 0-1$ was not quantified, the need to use a 60 μJ probe fluence is indicative of an extremely low population. Typically, molecules with allowed single-photon transitions can be routinely detected in the 10^7-10^8 cm^{-3} per quantum state range using LIF at 1−10 μJ fluence. Based on the photolysis laser flux density of 3×10^{15} cm^{-2} and the H_2S absorption cross section in Table 1, a nascent H-atom density of about 4×10^{12} cm^{-3} is formed. Even if only a fraction of the H-atom population reacts in 100 ns, a significant H + O_3 reaction branching fraction into the lower OH v levels would be easily detected. This evidence suggests that the yield of OH(v=0,1) is very small compared to the yield in the higher v levels. Also, the lower population in $v = 1$ relative to $v = 0$ implies that there may be a minimum in the OH nascent population distribution between $v = 1$ and $v = 6$, and that the low and high-v levels may be populated through different reaction mechanisms.

The complexity of the H + O_3 reaction dynamics is perhaps well exemplified by the recent study of Yu and Varandas,[13] who performed a detailed quasiclassical trajectory study of the H + O_3 reaction on a calculated H−O_3 potential energy surface over the range of translational energies between 0.015 and 0.75 eV. Their predicted OH nascent vibrational energy distribution is strikingly different from the experimental results, peaking in the $v = 4-5$ region instead of at $v = 9$. This suggests that the reaction surface needs to be improved. The present result could be used to help accomplish that task, by providing benchmark OH rotational and λ-doublet populations for the lower v levels, at a somewhat higher H-atom energy.

Thermalization of Fast H Atoms. To extend this experiment to lower energies it would be necessary to slow the H atoms prior to their reaction with O_3. This would much more closely reproduce the conditions at the mesopause region, where the H-atom population is thermalized at the 200 K ambient kinetic temperature. The photolysis method used herein is convenient and can be used to generate H from species such as H_2S or NH_3, the latter of which has a large photodissociation cross section at 193 nm to yield NH_2 + H.[28−30] Within the photolysis approach, the most obvious solution is to identify a bath gas which is efficient at slowing H atoms but does not appreciably affect the OH(v,N) distribution during that time.

Hydrogen atoms can be efficiently thermalized by adding bath gases which either are light or have internal degrees of freedom.[31] Park et al.[31] show that the H atoms arising from H_2S photolysis are nearly thermalized at 100 ns delay time in 10 Torr of He, O_2, or N_2. All three of these relaxers have shortcomings, however. While He is a very slow quencher of excited OH, in both the vibrational[32,33] and electronic (A state)[34] degrees of freedom, it is a fast relaxer of excited rotational populations.[35−38] For rotational relaxation of OH(v=0,N=1−12) by O_2 and N_2, Kliner and Farrow[39] recently measured smaller rate constants, in the mid-10^{-11} cm^3 s^{-1} range. N_2 is a much slower relaxer of vibrationally excited OH than O_2,[32] and only a moderately fast quencher of OH(A).[34] Thus, N_2 appears to be the most promising candidate to thermalize the H atoms without significantly relaxing the product OH or severely degrading the LIF sensitivity.

Summary

For the first time, OH(v=0,1) product populations from H + O_3 have been measured, using a laser pump−probe experi-

ment. Translationally excited H atoms were generated by photolyzing H_2S diluted in O_3, with the resultant OH detected via laser-induced fluorescence. Previous analysis of OH radiance data from the CIRRIS 1A space shuttle experiment has suggested that the H + O_3 reaction may significantly populate low v levels of the product OH, in addition to the known population of $v = 6-9$. Although higher v levels of OH were not detected in this experiment for direct comparison, an estimate of expected signal levels suggests that the yield of OH-(v=0,1) is very small compared to the total OH product yield. The OH v=1:v=0 population ratio is equal to 0.37, with the rotational level populations increasing gradually with N for both v levels. Intensity ratios in various rotational bands were used to unambiguously determine the λ-doublet population ratios, with F_1:F_2 equal to 1.03 and $\Pi(A')$:$\Pi(A'')$ equal to 1.34. The first rate constants for OH(A) collisional quenching by O_3 were determined, with the OH(A,v'=0,$N' \leq 25$)-O_3 quenching rate constants in the low-10^{-10} cm^3 s^{-1} range. The present results extend the measurements of the OH product distribution from H + O_3, and provide data that can be used to improve the accuracy of H−O_3 potential energy surface calculations.

Acknowledgment. We thank Dr. Richard A. Copeland for helpful suggestions. This material is based upon work supported by the National Science Foundation under Grant No. ATM-9714996. Support was also provided by the Air Force Office of Scientific Research under Project 2303ES, Task 92VS04COR.

References and Notes

(1) Shepherd, G. G.; Thuillier, G.; Gault, W. A. *J. Geophys. Res.* **1993**, *98*, 10725.

(2) Dodd, J. A.; Lipson, S. J.; Lowell, J. R.; Armstrong, P. S.; Blumberg, W. A. M.; Nadile, R. M.; Adler-Golden, S. M.; Marinelli, W. J.; Holtzclaw, K. W.; Green, B. D. *J. Geophys. Res.* **1994**, *99*, 3559.

(3) Morgan, F.; Yee, J. H.; Romick, G. J.; Carbary, J.; Swaminathan, P. K.; Morrison, D.; Anderson, D. E.; Paxton, L.; Meng, C. I. *Eos Trans. AGU* **1996**, *77(46)*, F529.

(4) Armstrong, P. S.; O′Neil, R. R.; Gardiner, H. A.; Gibson, J. J.; Zachor, A.; Woolston, T.; Kendra, M.; Lipson, S. J.; Vititoe, D. L.; Blumberg, W. A. M.; Dodd, J. A. *Eos Trans. AGU* **1997,** *78(17)*, S230.

(5) Cosby, P. C.; Slanger, T. G.; Osterbrock, D. E. *Eos Trans. AGU*, **1999**, *80(17)*, S252.

(6) Klenerman, D.; Smith, I. W. M. *J. Chem. Soc., Faraday Trans. 2* **1987**, *83*, 229.

(7) Ohoyama, H.; Kasai, T.; Yoshimura, Y.; Kimura, H.; Kuwata, K. *Chem. Phys. Lett.* **1985**, *118*, 263.

(8) Streit, G. E.; Johnston, H. S. *J. Chem. Phys.* **1976**, *64*, 95.

(9) Charters, P. E.; Macdonald, R. G.; Polanyi, J. C. *Appl. Opt.* **1971**, *10*, 1747.

(10) Xu, Z.; Koplitz, B.; Wittig, C. *J. Chem. Phys.* **1987**, *87*, 1062.

(11) Wight, C. A.; Leone, S. R. *J. Chem. Phys.* **1983**, *79*, 4823.

(12) Dupuis, M.; Fitzgerald, G.; Hammond, B.; Lester, W. A.; Schaefer, H. F., III *J. Chem. Phys.* **1986**, *84*, 2691.

(13) Yu, H. G.; Varandas, A. J. C. *J. Chem. Soc., Faraday Trans.* **1997**, *93*, 2651.

(14) Aker, P. M.; O′Brien, J. J. A.; Sloan, J. J. *Chem. Phys.* **1986**, *104*, 421.

(15) Kleinermanns, K.; Wolfrum, J. *J. Chem. Phys.* **1984**, *80*, 1446.

(16) Copeland, R. A., private communication, 1998.

(17) Luque, J.; Crosley, D. R. LIFBASE: Database and Spectral Simulation Program (Version 1.5); SRI International Report MP 99-009, 1999.

(18) Luque, J.; Crosley, D. R. *J. Chem. Phys.* **1998**, *109*, 439.

(19) Press: W. H.; Flannery, B. P.; Teukolsky, S. A.; Vetterling, W. T. *Numerical Recipes*, 2nd ed.; Cambridge University Press: New York, 1992.

(20) Lehmann, K. K.; Scherer, G. J.; Klemperer, W. *J. Chem. Phys.* **1982**, *77*, 2853.

(21) Jacobson, M. P. *Robust Baseline Estimation*; Ph.D. Thesis, Massachusetts Institute of Technology, 1999; Chapter 5.

(22) Ruckstuhl, A.; Jacobson, M. P.; Field, R. W.; Dodd, J. A., manuscript in preparation.

(23) Demtröder, W. *Laser Spectroscopy*, 2nd ed.; Springer: New York, 1996.

(24) Melen, F.; Sauval, A. J.; Grevesse, N.; Farmer, C. B.; Servais, Ch.; Delbouille, L.; Roland, G. *J. Mol. Spectrosc.* **1995**, *174*, 490.

(25) Coxon, J. A. *Can. J. Phys.* **1980**, *58*, 933.

(26) Alexander, M. H., et al. *J. Chem. Phys.* **1988**, *89*, 1749.

(27) DeMore, W. B.; Sander, S. P.; Howard, C. J.; Ravishankara, A. R.; Golden, D. M.; Kolb, C. E.; Hampson, R. F.; Kurylo, M. J.; Molina, M. J. "Chemical Kinetics and Photochemical Data for Use in Stratospheric Modeling", eval. 11, JPL Publ. 94-26, 1994.

(28) Okabe, H. *Photochemistry of Small Molecules*; Wiley-Interscience: New York, 1978.

(29) Back, R. A.; Koda, S. *Can. J. Chem.* **1977**, *55*, 1387.

(30) Donnelly, V. M.; Baronavski, A. P.; McDonald, J. R. *Chem. Phys.* **1979**, *43*, 271.

(31) Park, J.; Shafer, N.; Bersohn, R. *J. Chem. Phys.* **1989**, *91*, 7861.

(32) Dyer, M. J.; Knutsen, K.; Copeland, R. A. *J. Chem. Phys.* **1997**, *107*, 7809.

(33) Lengel, R. K.; Crosley, D. R. *J. Chem. Phys.* **1978**, *68*, 5309.

(34) Hogan, P.; Davis, D. D. *J. Chem. Phys.* **1976**, *64*, 3901.

(35) Schreel, K.; Schleipen, J.; Eppink, A.; ter Meulen, J. J. *J. Chem. Phys.* **1993**, *99*, 8713.

(36) Jorg, A.; Esposti, A. D.; Werner, H.-J. *J. Chem. Phys.* **1990**, *93*, 8757.

(37) Jorg, A.; Meier, U.; Kohse-Hoinghaus, K. *J. Chem. Phys.* **1990**, *93*, 6453.

(38) Zizak, G.; Petrucci, G. A.; Stevenson, C. L.; Windfordner, J. D. *Appl. Opt.* **1991**, *30*, 5270.

(39) Kliner, D. A. V.; Farrow, R. L. *J. Chem. Phys.* **1999**, *110*, 412.

(40) Turco, R. P. *Geophys. Surveys* **1975**, *2*, 153.

(41) Klee, S.; Gericke, K.-H.; Comes, F. J. *Chem. Phys. Lett.* **1985**, *118*, 530.